Asteroid lightcurve inversion with Lommel-Seeliger ellipsoids

Karri Muinonen[a,b], Olli Wilkman[a], Alberto Cellino[c], Xiaobin Wang[d], and Yibo Wang[d1]

[a] *Department of Physics, Gustaf Hällströmin katu 2a, P.O. Box 64, FI-00014 U. Helsinki, Finland*

[b] *Finnish Geospatial Research Institute FGI, Geodeetinrinne 2, FI-02430 Masala, Finland*

[c] *INAF, Osservatorio Astrofisico di Torino, Strada Osservatorio 20, I-10025 Pino Torinese (TO), Italia*

[d] *Yunnan Observatories, CAS, P.O. Box 110, Kunming 650011, China*

Abstract

We derive initial rotation, shape, and scattering properties for asteroids from sparse and dense photometry based on the so-called Lommel-Seeliger ellipsoid (LS ellipsoid). Due to their analytical disk-integrated brightness, LS ellipsoids allow for fast rotation-period, pole-orientation, and shape analyses, as well as efficient virtual-observation Markov-chain Monte Carlo solutions (MCMC). We apply the methods to simulated sparse Gaia photometry, as well as to groundbased photometry composed of dense lightcurves. For a specific Gaia simulation, we make use of a state-of-the-art numerical reflection coefficient developed for particulate surfaces, and utilize the LS-ellipsoid in the inversion of the simulated data. We conclude that, in a majority of cases, inversion with LS-ellipsoids results in satisfactory initial retrievals of the parameters. Finally, we give a single-scattering phase function that, for a spherical asteroid, results in a disk-integrated phase function of the form of the H,G_1,G_2 photometric phase function.

Keywords: asteroids, near-Earth objects, lightcurve inversion, Lommel-Seeliger ellipsoid, Lommel-Seeliger reflection coefficient, particulate-medium reflection coefficient, Markov chain Monte Carlo; Gaia

[1] Corresponding author; Fax: +358 2941 50610, Email: karri.muinonen@helsinki.fi

1. Introduction

The rotation period, pole orientation, and three-dimensional shape of an asteroid is derived from photometric lightcurves observed in a number of apparitions with varying illumination and observation geometries (e.g., [1, 2, 3]). It is customary to estimate the rotation period with a regular initial shape model and a small number of trial pole orientations. Once the period is available, the pole orientation and shape can be refined with a general convex shape model. In what follows, we focus on the initial inverse problem exhibited by sparse photometry or a number of dense lightcurves observed in a limited set of viewing geometries.

The morphology of asteroid lightcurves is affected by a variety of macroscopic and microscopic properties of the surface. The overall shape plays certainly a major role and can be responsible for significant changes in the lightcurve of the same object observed at different epochs in a variety of observing conditions (aspect and phase angles). This was already mentioned by Cellino et al. [4], in which an eight-octant model for asteroid shapes (the so-called "Cellinoid shape model") was first introduced. Some recent analyses [5] suggest that this shape model can be conveniently applied to the problem of inversion of asteroid lightcurves.

The inversion of asteroid photometric data can become even more difficult when one does not have at disposal full lightcurves, but only sparse photometric "snapshots" of an object taken at different epochs. This is exactly the problem that must be faced in the case of the inversion of Gaia photometric data, the average number of Gaia measurements being of the order of 70 per object. In the case of Gaia, there is the additional complication of the large number of objects to be processed (of the order of 10^5, and the challenge of the limited computing time available to accomplish this task in the framework of the Gaia data reduction activities. The solution that has been found is the application of a genetic algorithm that assumes the bodies to have regular triaxial ellipsoid shapes and finds the best combination of axial ratios, rotation period, and pole orientation that produces the best fit to the data. In so doing, also a linear variation of magnitude as a function of phase angle is assumed to take place [6].

The results of the ellipsoid approach have been found to be satisfactory according to many numerical simulations. The most recent analysis has been

published by Santana-Ros et al. [7], who performed several sets of simulations for 10,000 asteroids having different periods, poles, and shapes. The effects of different photometric errors affecting the data was also simulated. The results confirmed the reliability of the inversion algorithm, and showed that, as expected, the obtained results are worse when inverting asteroids having quasi-spherical shapes and/or low pole latitudes. The latter effect is caused by the intrinsically small photometric variations occurring in these cases. Santana-Ros et al. also analyzed the effect of having at disposal, in addition to sparse Gaia data, a full lightcurve obtained from ancillary ground-based observations. The results suggest that it should be possible in this way to reduce the number of wrong solutions for asteroids having less than 50 photometric data points.

We focus on the initial derivation of the rotational period and pole orientation with the help of the Lommel-Seeliger ellipsoid (LS-ellipsoid), a triaxial ellipsoid with a Lommel-Seeliger surface reflection coefficient. The disk-integrated photometric brightness for the LS-ellipsoid is available analytically [8], warranting efficient computation of lightcurves and fast inverse methods.

With modern computers and the LS-ellipsoid, the rotation period, pole orientation, and ellipsoidal shape can be derived simultaneously, e.g., by using a genetic algorithm (as described above and in Cellino et al. [9]. Here we offer an alternative approach and proceed systematically as follows. First, the rotation period is scanned across its relevant range with a resolution $P_0^2/2T$ given by a tentative period estimate P_0 and the time interval T spanned by the photometric data. This is typically carried out for a small number of different pole orientations on the unit sphere. For each rotation period and pole orientation, the pole orientation itself, rotational phase, and axial ratios (also, optionally, the scattering parameters) are optimized with the help of the Nelder-Mead downhill simplex method. Although the shape optimization can suffer from getting stuck in local minima, overall, the rotation period is fairly reliably obtained by the initial scanning.

Second, for the rotation period obtained, the pole orientation can be mapped with a high resolution pertaining to a few degrees on the unit sphere, with downhill simplex optimization for the rotation period, rotational phase, and axial ratios (again, optionally also the scattering parameters) in the case of each trial pole orientation. Third, after mapping the pole orientation, the regimes of minima are evident, and analyses can be focused on each of the regimes separately. Now all the parameters can be optimized to obtain the best single fit to the data.

Next, in order to allow for an efficient Markov-chain Monte Carlo analysis (MCMC) in the proximity of the best-fit solution, we generate virtual observations, by adding random noise to the observations, and repeat the optimization for the parameters by using the virtual data (see [10, 11]). The differences of what we call the virtual least-squares parameters can then be utilized as proposals in the final MCMC sampling of the parameters. At the end, we obtain a description of the probability density function for the period, pole, rotational phase, and ellipsoid axial ratios (also, optionally, the scattering parameters) in the neighborhood of the best-fit parameters. The MCMC analysis can be repeated for each different solution regime separately and mutual weights of the separate regimes can be derived. Uniform MCMC sampling of the phase space can be carried out in a way similar to that in asteroid orbital inversion (see [12]).

The Lommel-Seeliger reflection coefficient omits the shadowing effects due to the random rough, particulate geometry of the regolith. These effects are accounted for by Wilkman et al. [13], Muinonen et al. [14], and Parviainen & Muinonen [15, 16]. They introduce fractional-Brownian-motion surface roughness on a close-packed plane-parallel medium of finite, spherical particles with a size distribution. In the present work, the particulate-medium reflection coefficient by Wilkman et al. is introduced for asteroid lightcurve-inversion studies via a direct simulation of sparse photometry mimicking that from the Gaia mission.

The LS-ellipsoid allows us to study the effect of changing viewing geometry on the photometric phase curves of nonspherical asteroids. We model the LS-ellipsoid phase function with the help of the H, G_1, G_2 phase function developed for asteroid phase curve studies [17] and adopted by the International Astronomical Union in 2012 as the new phase function in the official asteroid magnitude system.

The contents of the present work are as follows. In Section 2, we describe the Lommel-Seeliger and particulate-medium reflection coefficients for close-packed media. We give the analytical disk-integrated brightness for the triaxial ellipsoid with a Lommel-Seeliger reflection coefficient. In Section 3, we describe the Markov-chain Monte Carlo methods (MCMC), and, in particular, the concept of the so-called virtual least-squares solutions in defining the MCMC proposal probability densities. Section 4 concentrates on the numerical methods, including a summary for the computation of the particulate-medium reflection coefficient and the robust derivation of least-squares solutions using the downhill simplex method. In Section 5, we ap-

ply the inverse methods to both dense and sparse lightcurves, especially, to ground-based observations of main-belt asteroids (e.g., [10] and simulations for the Gaia mission [7].

2. Photometry

2.1. Diffuse reflection coefficient

The reflection coefficient R of a surface element relates the incident flux density πF_0 and the emergent intensity I as

$$\begin{aligned} I(\mu,\phi,;\mu_0,\phi_0) &= \mu_0 R(\mu,\phi,;\mu_0,\phi_0)F_0, \\ & \quad \mu_0=\cos\iota, \quad \mu=\cos\epsilon, \end{aligned} \tag{1}$$

where ι and ϵ are the angles of incidence and emergence as measured from the outward normal vector of the surface element, and ϕ_0 and ϕ are the corresponding azimuthal angles. It is customary to measure ϕ so that the backscattering direction (or light-source direction) is with $\phi = 0°$. Thus, with the typical assumption of a geometrically isotropic surface, ϕ_0 is obsolete. The reflection coefficient obeys the reciprocity relation

$$R(\mu,\mu_0,\phi) = R(\mu_0,\mu,2\pi-\phi). \tag{2}$$

The Lommel-Seeliger reflection coefficient (subscript LS) is (e.g., [18]),

$$R_{\rm LS}(\mu,\mu_0,\phi) = \frac{1}{4}\tilde{\omega}P(\alpha)\frac{1}{\mu+\mu_0}, \tag{3}$$

where $\tilde{\omega}$ is the single-scattering albedo, P is the single-scattering phase function, and α is the phase angle, the angle between the Sun (light source) and the observer as seen from the object. The Lommel-Seeliger reflection coefficient, the first-order multiple-scattering approximation from the radiative-transfer theory (e.g., [19]), is applicable to weakly scattering media: the intensity terms $[\tilde{\omega}^k]$, $k \geq 2$ are assumed negligible. $\tilde{\omega}$ is the fraction of the incident flux scattered by the single scatterer ($0 \leq \tilde{\omega} \leq 1$). The present single scatterers can be single particles or volume elements within the medium. In scalar radiative transfer omitting polarization effects, the scattering phase function P provides the angular distribution of scattered light in an individual interaction and is normalized so that

$$\int_{(4\pi)} \frac{d\Omega}{4\pi} P(\alpha) = 1. \tag{4}$$

For a dark particulate medium composed of absorbing particles (small $\tilde{\omega}$) and accounting for shadowing effects through numerical simulations [13], the reflection coefficient is given by

$$R_{\rm PM}(\mu,\mu_0,\phi) \;=\; \frac{1}{4}\tilde{\omega}P(\alpha)S(\alpha,\mu,\mu_0)\frac{1}{\mu+\mu_0}, \tag{5}$$

where the subscript "PM" stands for the particulate medium and S denotes the shadowing function, a correction to the Lommel-Seeliger reflection coefficient in order to reproduce the numerical coefficient computed for the particulate media. In practice, S is normalized as

$$S(\alpha=0^\circ,\mu,\mu_0) \;\approx\; 2, \tag{6}$$

an indication of the shadowing mechanism allowing rays incident on particles to emerge, after a scattering process, in the backward scattering direction along their paths of incidence.

2.2. Disk-integrated brightness

The disk-integrated brightness L equals the surface integral

$$\begin{aligned} L(\alpha) &= \int_{A_+} dA\ \mu I(\mu,\mu_0,\alpha) \\ &= \int_{A_+} dA\ \mu\mu_0 R(\mu,\mu_0,\alpha)F_0, \end{aligned} \tag{7}$$

where A_+ stands for the part of the surface that is both illuminated by the light source and visible to the observer. For a nonspherical asteroid, L can depend strongly on the orientation of the asteroid with respect to the scattering plane, where L is measured.

For a spherical asteroid with diameter D,

$$L(\alpha) \;=\; \frac{1}{4}D^2\int_{\Omega_+} d\Omega\ \mu\mu_0 R(\mu,\mu_0,\alpha)F_0, \tag{8}$$

where Ω_+ stands for the part of the unit sphere both illuminated and observable. For the Lommel-Seeliger reflection coefficient, the computation of L in Eq. 8 can be carried out analytically in a coordinate system, where

the Sun and the observer are in the xy-plane. We obtain the disk-integrated brightness

$$\begin{aligned} L_{\rm LS}(\alpha) &= \frac{1}{32}\pi F_0 D^2 \tilde{\omega} P(\alpha)[1 - \sin\frac{1}{2}\alpha \ \tan\frac{1}{2}\alpha \ \ln(\cot\frac{1}{4}\alpha)], \\ \Phi_{\rm LS}(\alpha) &= \frac{L_{\rm LS}(\alpha)}{L_{\rm LS}(0^\circ)} = 1 - \sin\frac{1}{2}\alpha \ \tan\frac{1}{2}\alpha \ \ln(\cot\frac{1}{4}\alpha), \end{aligned} \tag{9}$$

where we have also given the phase function $\Phi_{\rm LS}(\alpha)$ normalized to unity at zero phase angle.

Consider next an ellipsoidal shape model for an asteroid with the semiaxes a, b, and c, and denote $C = {\rm diag}(a^{-2}, b^{-2}, c^{-2})$ (C is a diagonal 3×3 matrix). Let $\mathbf{e}_\odot$ and $\mathbf{e}_\oplus$ be the unit vectors in the directions of the Sun and the observer, respectively, as seen in the principal axes reference frame of the ellipsoid.

For the computation of the disk-integrated brightness, we define three sets of auxiliary quantities. First, the solar phase angle follows from

$$\cos\alpha = \mathbf{e}_\odot \cdot \mathbf{e}_\oplus. \tag{10}$$

Second, we define two vector-matrix products $S_\odot$ and $S_\oplus$ as well as an angle α' so that

$$\begin{aligned} S_\odot &= \sqrt{\mathbf{e}_\odot^{\rm T} C \mathbf{e}_\odot}, \\ S_\oplus &= \sqrt{\mathbf{e}_\oplus^{\rm T} C \mathbf{e}_\oplus}, \\ \cos\alpha' &= \frac{\mathbf{e}_\odot^{\rm T} C \mathbf{e}_\oplus}{S_\odot S_\oplus}, \\ \sin\alpha' &= \sqrt{1 - \cos^2\alpha'}. \end{aligned} \tag{11}$$

Third, we define an amplitude S and an angle λ' so that

$$\begin{aligned} S &= \sqrt{S_\odot^2 + S_\oplus^2 + 2 S_\odot S_\oplus \cos\alpha'}, \\ \cos\lambda' &= \frac{S_\odot + S_\oplus \cos\alpha'}{S}, \\ \sin\lambda' &= \frac{S_\oplus \sin\alpha'}{S}. \end{aligned} \tag{12}$$

The disk-integrated brightness of a Lommel-Seeliger ellipsoid is then given by

$$L(\alpha) = \frac{1}{8}\,\pi F_0 \tilde{\omega} P(\alpha)\; abc \frac{S_\odot S_\oplus}{S}\; \{\cos(\lambda' - \alpha') + \cos\lambda' + \sin\lambda' \sin(\lambda' - \alpha') \ln\left[\cot\frac{1}{2}\lambda' \cot\frac{1}{2}(\alpha' - \lambda')\right]\Big\}. \quad (13)$$

For more information about the disk-integrated brightness and photocenter of a Lommel-Seeliger ellipsoid, see the work by Muinonen and Lumme [8].

Consider next the single-scattering albedo $\tilde{\omega}$ and phase function $P(\alpha)$. Common knowledge on asteroid phase curves suggests that the disk-integrated brightness phase function ought to be close to the H,G_1,G_2 phase function $\Phi_{HG_1G_2}$ [17]. Furthermore, the geometric albedo p of a Lommel-Seeliger sphere is

$$p = \frac{1}{8}\tilde{\omega} P(0^\circ). \quad (14)$$

It is now reasonable to assume that the model

$$\frac{1}{8}\tilde{\omega} P(\alpha) = p \frac{\Phi_{HG_1G_2}(\alpha)}{\Phi_{\rm LS}(\alpha)} \quad (15)$$

can serve well in asteroid phase-curve analyses. Such modeling results in phase-curve variations from one apparition to another. The normalization to the LS phase curve of a spherical asteroid is convenient, especially for inverse methods, as it is independent of the ellipsoid axial ratios. The resulting variations for ellipsoids are a subject of study below in Sect. 5.

Finally, we can introduce a relative phase function that is locally linear in brightness as

$$\frac{1}{8}\tilde{\omega} P(\alpha) \propto \frac{1 - k_0\alpha)}{\Phi_{\rm LS}(\alpha)}, \quad (16)$$

where k_0 is the slope of the phase function. The locally linear model is useful for the analyses of the Gaia photometry that is constrained to phase angles of approximately $15^\circ \leq \alpha \leq 50^\circ$. Note that, due to the normalization to the phase function of the LS-sphere, for the LS-ellipsoids, there will be variations from the linearity depending on the viewing geometry.

3. Inverse methods

3.1. Statistical inverse problem

We describe the rotation, size, shape, and scattering parameters of an asteroid at a given epoch t_0 by the vector $\mathbf{P} = (P, \lambda, \beta, \varphi_0, a, b, c, p, G_1, G_2, D)^T$ (T is transpose), where the parameters are, respectively, the rotation period, ecliptic pole longitude, ecliptic pole latitude, rotational phase at t_0, three ellipsoid semiaxes in relative units (typically, $a = 1$), geometric albedo, two parameters of the H,G_1,G_2 phase function, and the first ellipsoid axis in physical units (diameter for a spherical asteroid).

Let $p_{\rm p}$ be the a posteriori probability density function (p.d.f.) for the parameters. Within the Bayesian framework (cf., [20]), $p_{\rm p}$ is proportional to the a priori and observational error p.d.f.s $p_{\rm pr}$ and p_ϵ, the latter being evaluated for the "Observed-Computed" residuals (O-C) $\Delta\mathbf{L}(\mathbf{P})$ of the disk-integrated brightnesses,

$$\begin{aligned} p_{\rm p}(\mathbf{P}) &\propto p_{\rm pr}(\mathbf{P}) p_\epsilon(\Delta\mathbf{L}(\mathbf{P})), \\ \Delta\mathbf{L}(\mathbf{P}) &= \mathbf{L}_{\rm obs} - \mathbf{L}(\mathbf{P}), \end{aligned} \tag{17}$$

where $\mathbf{L}_{\rm obs}$ and $\mathbf{L}$ denote the observations and the computed brightnesses. It is currently assumed that p_ϵ is Gaussian and that $p_{\rm pr}$ is constant. The final a posteriori p.d.f. is thus

$$\begin{aligned} p_{\rm p}(\mathbf{P}) &\propto \exp\left[-\frac{1}{2}\chi^2(\mathbf{P})\right], \\ \chi^2(\mathbf{P}) &= \Delta\mathbf{L}^T(\mathbf{P}) \Lambda^{-1} \Delta\mathbf{L}(\mathbf{P}), \end{aligned} \tag{18}$$

where χ^2 measures O-C distance in terms of the error model and Λ denotes the covariance matrix of the errors. Lacking knowledge of the correlations among the observations, we assume that Λ is diagonal and that

$$\Lambda_{ii} = \sigma_i^2, \quad i = 1, 2, 3, \ldots, N, \tag{19}$$

where σ_i is the error standard deviation of the ith observation and N is the total number of observations. Thus,

$$\chi^2(\mathbf{P}) = \sum_{i=1}^{N} \frac{1}{\sigma_i^2} \left[L_{{\rm obs},i} - L_i(\mathbf{P})\right]^2 . \tag{20}$$

In practice, the observation vector is composed of a number of lightcurves with their varying numbers of brightnesses,

$$\begin{aligned} \chi^2(\mathbf{P}) &= \sum_{i=1}^{N_0} \sum_{j=1}^{N_i} \frac{1}{\sigma_{ij}^2} \left[L_{\mathrm{obs},ij} - L_{ij}(\mathbf{P}) \right]^2, \\ N &= \sum_{i=1}^{N_0} N_i, \end{aligned} \tag{21}$$

where N_0 is the number of lightcurves, N_i is the number of observations in the ith lightcurve, and σ_{ij} is the error standard deviation of the jth observation in the ith lightcurve. Furthermore, we are currently dealing with relative photometry, that is, we do not utilize the absolute brightness difference between different lightcurves. Accordingly, for the relative treatment, we have

$$\begin{aligned} \chi^2(\mathbf{P}) &= \sum_{i=1}^{N_0} \frac{1}{\bar{L}_{\mathrm{obs},i}^2} \sum_{j=1}^{N_i} \frac{1}{\sigma_{ij}^2} \left[L_{\mathrm{obs},ij} - L_{ij}(\mathbf{P}) \right]^2, \\ \bar{L}_{\mathrm{obs},i} &= \frac{1}{N_i} \sum_{j=1}^{N_i} L_{\mathrm{obs},ij}, \end{aligned} \tag{22}$$

where $\bar{L}_{\mathrm{obs},i}$ is the mean brightness of the ith observed lightcurve.

3.2. Markov-chain Monte Carlo sampling

MCMC methods (cf., [21]) provide the practical means for sampling complicated, unnormalized p.d.f.s as in Eq. 18. The Metropolis-Hastings algorithm, utilized presently, is based on the computation of the ratio a_r:

$$a_r = \frac{p_{\mathrm{p}}(\mathbf{P}') p_{\mathrm{t}}(\mathbf{P}_j; \mathbf{P}')}{p_{\mathrm{p}}(\mathbf{P}_j) p_{\mathrm{t}}(\mathbf{P}'; \mathbf{P}_j)}. \tag{23}$$

Here $\mathbf{P}_j$ and $\mathbf{P}'$ denote the current and proposed parameters in a Markov chain, respectively, and $p_{\mathrm{t}}(\boldsymbol{P}'; \mathbf{P}_j)$ is the proposal p.d.f. from $\mathbf{P}_j$ to $\boldsymbol{P}'$ (subscript t stands for transition). The proposed parameters $\mathbf{P}'$ are accepted, that is $\mathbf{P}_{j+1} = \mathbf{P}'$, with the probability of

$$p' = \min(1, a_r). \tag{24}$$

If the parameters $\mathbf{P}'$ are rejected, $\mathbf{P}_{j+1} = \mathbf{P}_j$. After a number of transitions in the so-called burn-in phase, the Markov chain, in the case of success, converges to sample the target p.d.f. $p_{\rm p}$. For convergence monitoring, there are various diagnostics tools available (see, e.g., [22]).

In the virtual-observation MCMC method, earlier developed for asteroid orbital inversion [11], the potentially complex solution phase space is first characterized statistically to arrive at a relevant proposal p.d.f. In what follows, we describe the essential features of the virtual-observation MCMC method for lightcurve inversion.

A set of virtual observations $\mathbf{L}_{\rm v}$ is generated from the original observations $\mathbf{L}_{\rm obs}$ through the addition of Gaussian random errors $\boldsymbol{\epsilon}_{\rm v}$ with zero means and covariance matrix $\Lambda_{\rm v}$,

$$\mathbf{L}_{\rm v} \;=\; \mathbf{L}_{\rm obs} + \boldsymbol{\epsilon}_{\rm v}. \tag{25}$$

Thereafter, least-squares parameters $\mathbf{P}_{\rm v}$ are obtained by minimizing

$$\chi^2_{\rm v}(\mathbf{P}) \;=\; \left[\mathbf{L}_{\rm v} - \mathbf{L}(\mathbf{P})\right]^{\rm T} \left(\Lambda + \Lambda_{\rm v}\right)^{-1} \left[\mathbf{L}_{\rm v} - \mathbf{L}(\mathbf{P})\right], \tag{26}$$

where the covariance matrix $\Lambda + \Lambda_{\rm v}$ reflects the presence of both real and virtual errors.

As $\boldsymbol{\epsilon}_{\rm v}$ is a vector of Gaussian random variables, what we term the virtual least-squares parameters $\mathbf{P}_{\rm v}$ are random variables, too. The p.d.f. for $\mathbf{P}_{\rm v}$ is formally the N-dimensional integral

$$p(\mathbf{P}_{\rm v}) \;=\; \int d\mathbf{L}_{\rm v} \delta(\mathbf{P}_{\rm v} - \mathbf{P}_{\rm v}(\mathbf{L}_{\rm v})) p(\mathbf{L}_{\rm v}), \tag{27}$$

where $p(\mathbf{L}_{\rm v})$ is the Gaussian p.d.f. for the virtual observations and δ is Dirac's Delta function. The symmetric proposal p.d.f. is defined as the $2(N + N_{\rm p})$-dimensional integral ($N_{\rm p}$ is the number of parameters)

$$p_{\rm t}(\Delta\mathbf{P}) \;=\; \int\int d\mathbf{P}_{\rm v} d\mathbf{P}'_{\rm v}\; \delta\left[\Delta\mathbf{P} - (\mathbf{P}_{\rm v} - \mathbf{P}'_{\rm v})\right] p(\mathbf{P}_{\rm v}) p(\mathbf{P}'_{\rm v}), \tag{28}$$

where the integration over $N_{\rm p}$ parameters results in the $(2N+N_{\rm p})$-dimensional convolution integral

$$p_{\rm t}(\Delta\mathbf{P}) \;=\; \int d\mathbf{P}_{\rm v}\; p(\mathbf{P}_{\rm v}) p(\mathbf{P}_{\rm v} - \Delta\mathbf{P}). \tag{29}$$

It is noteworthy that, due to the symmetry of the proposal p.d.f., these integrals need not be numerically evaluated and the proposal can be computed by repeating the determination of the virtual least-squares parameters and adopting the difference in the parameters as the proposed transition.

Whereas the procedure above meets the mathematical requirements for a symmetric proposal p.d.f. in a Metropolis-Hastings algorithm [21], it can be computationally cumbersome to generate such proposals during the MCMC sampling. A straightforward alternative, implemented here, is to compute large numbers of parameter differences $\Delta\mathbf{P}$ before the MCMC sampling.

Repeat the generation of virtual observation sets $\mathbf{L}_\mathrm{v}$ and the derivation of $\mathbf{P}_\mathrm{v}$ until there are $N_\mathrm{v} \gg 1$ sets of parameters $\mathbf{P}_\mathrm{v}^{(j)}$ $(j = 1, 2, 3 \ldots, N_\mathrm{v})$. Parameter differences are then readily available from

$$\Delta\mathbf{P}_{jk} = \mathbf{P}_{\mathrm{v},j} - \mathbf{P}_{\mathrm{v},k}, \qquad j, k = 1, 2, 3 \ldots, N_\mathrm{v};\ j \neq k. \tag{30}$$

These differences offer a finite number of relevant transitions from one parameter set to another in the phase space. Notice that there are of the order of $N_\mathrm{v} \times N_\mathrm{v}$ differences available, that is, a number that can become extremely large for reasonable values of N_v. Strictly, any pair of parameters consumed for a difference should be replaced by a new pair of parameters computed as described above.

The ratio a_r for the decision criterion is simply

$$a_r \quad = \quad \frac{p_\mathrm{p}(\mathbf{P}')}{p_\mathrm{p}(\mathbf{P}_j)}. \tag{31}$$

The proposals can now be computed during the MCMC sampling using the N_v virtual least-squares element sets $\boldsymbol{P}'_{\mathrm{v},j}$. In the limit of $N_\mathrm{v} \to \infty$, the discrete approach coincides with the aforedescribed approach of computing differences in virtual least-squares elements during the actual MCMC sampling.

Finally, in order to enhance the robustness of the virtual-observation MCMC sampler, we provide an MCMC importance sampler as follows. Instead of drawing random samples from the a posteriori probability density for the parameters as above, we can draw random samples of parameters from a uniform distribution within a given regime in $\chi^2(\mathbf{P})$, say,

$$\Delta\chi^2 = \chi^2(\mathbf{P}) - \chi^2(\mathbf{P}_0) \quad \leq \quad \Delta\chi^2_\mathrm{c}, \tag{32}$$

where $\mathbf{P}_0$ denotes the least-squares parameters and the critical $\Delta\chi^2_{\rm c}$ is set on the basis of the number of parameters. For the present inverse problem, we may assume

$$30 \leq \Delta\chi^2_{\rm c} \leq 100. \tag{33}$$

For the acceptance and rejection of parameters, we have

$$a_r \;=\; \begin{cases} 0, & \Delta\chi^2 \geq \Delta\chi^2_{\rm c}, \\ \text{const.} \neq 0, & \Delta\chi^2 < \Delta\chi^2_{\rm c}, \end{cases} \tag{34}$$

that is, transitions are always accepted within the given $\Delta\chi^2_{\rm c}$ regime and never out of the regime.

4. Numerical methods

4.1. Computation of $R_{\rm PM}$

In Eq. 5, we have adjusted the Lommel-Seeliger model with an additional term, the shadowing function S, to take into account the effect of surface porosity and roughness. We have computed the shadowing function numerically using a ray-tracing simulation, discretizing it over (ι, ϵ, ϕ). This computation is time-consuming, but once the discretized S has been computed for one surface, it can be saved into a file and used efficiently [13].

We have used a medium consisting of spheres with Lommel-Seeliger scattering surfaces with an isotropic phase function as a tool to compute S. We have used a ray-tracing simulation to compute the intensity scattered by such a surface, $\hat{I}_{\rm RT}$.

In the limit of a very sparse packing, the ray-tracing is equivalent to a semi-infinite Lommel-Seeliger scattering surface, in which the single-scattering phase function happens to be the disk-integrated brightness of a Lommel-Seeliger sphere (Eq. 9). The shadowing function S is defined as the ratio between the ray-tracing result and a Lommel-Seeliger reflecting medium. Thus, S can be understood to be the ratio of the mutually shadowing particles of the ray-tracing simulation to a theoretical medium composed of similar particles which now shadow each other.

For the theoretical Lommel-Seeliger surface, the brightness is

$$I_{\rm LS} \;=\; \frac{\hat{\omega}_V}{4} P_{\rm LS}(\alpha) \frac{\mu_0}{\mu_0 + \mu}, \tag{35}$$

where the volume-element albedo is $\hat{\omega}_V = \frac{2}{3}(1 - \log 2)\omega_0$, where ω_0 is the single-scattering albedo used in the simulation. $P_{\rm LS}$ is the disk-integrated brightness of a Lommel-Seeliger scattering sphere, but now normalized so that

$$\int_{4\pi} \frac{P_{\rm LS}}{4\pi} {\rm d}\Omega \;\; = \;\; 1. \tag{36}$$

The shadowing function S is now found as the ratio between the ray-tracing result and the theoretical value,

$$S \;\; = \;\; \frac{\hat{I}_{\rm RT}}{I_{\rm LS}} = \frac{1}{4}\frac{\mu_0 + \mu}{\mu_0}\frac{\hat{I}_{\rm RT}}{\hat{\omega}_V P_{\rm LS}(\alpha)}. \tag{37}$$

The S function computed this way is approximately independent of the scattering model chosen for the individual spheres (in our case Lommel-Seeliger). This approximation of S becomes worse as the packing density of the surface increases.

4.2. LS-ellipsoid computations

The aforedescribed direct and inverse photometric methods based on the LS-ellipsoid have been developed into a Fortran77 software package composed of a little over 3000 lines of program code with comments. The model parameters are the rotation period P, the ecliptic pole longitude and latitude λ and β, the rotational phase φ_0 (at a given epoch t_0), the ellipsoid axes a, b, and c, the geometric albedo p, the G_1 and G_2 parameters of the phase function (alternatively, G_{12}), and the ellipsoid axis a in kilometers.

As for the direct methods, the software package provides a tool to generate a viewing geometry. It also provides a tool for the computation of disk-integrated brightnesses (Eq. 13) and photocenters [8] for input parameters and observation dates and geometries. It is possible to add random errors to the disk-integrated brightnesses and to simulate realistic lightcurve data for LS-ellipsoids.

As for the inverse methods, first, systematic scanning of the rotation period is offered with a resolution $< P^2/2T$ (where T denotes the observational time interval) with optimization for pole orientation, shape, and scattering parameters for predefined initial pole orientations and shape parameters. Second, systematic scanning of pole orientation is offered over the full solid angle with optimization of rotation period, shape, and scattering parameters for predefined initial parameters. For both period and pole scanning,

the optimization is carried out with a flexible Nelder-Mead downhill simplex method (Press et al. 1992). Period scanning can take of the order of hours of computing time on a single core, but can be efficiently parallelized for multiple cores. Pole scanning with a resolution of approximately 3° on the unit sphere and with optimization for 5-6 parameters at each candidate pole takes typically only minutes of computing time on a single core.

Third, using the simplex algorithm, the least-squares rotation, shape, and scattering parameters opted are derived for the given set of observations. There are three alternative error models: a single error standard deviation can be specified at input, individual rms-based error standard deviations can be utilized for each lightcurve (with iteration), and the individual error standard deviations can be increased to account for systematical residual trends due to the ellipsoid shape model, that is, due to a regular instead of an irregular shape model. The last option is analogous to the slip factor introduced in asteroid orbital inversion by Muinonen and Bowell [20].

Fourth, again using the simplex algorithm, least-squares spin, shape, and scattering parameters are derived, first, for the true observations, and, second, for a specified number of virtual observation sets generated by adding Gaussian random errors to the true observations. The tool thus generates virtual least-squares parameters to be utilized in drawing samples from the proposal probability density in the MCMC and MCMC-importance methods below. There needs to be at least an order of magnitude more virtual least-squares solutions as there are MCMC or MCMC importance samples in the methods below. The error model can be any one of the three described above and the user can specify the standard deviation for the additional Gaussian errors. Typically, the generation of 10^4 or more virtual parameter sets requires of the order of minutes to tens of minutes of computing time on a single core.

Fifth, MCMC sampling is carried out for the rotation, shape, and scattering parameters opted with the help of the virtual least-squares solutions from the previous tool. Finally, sixth, MCMC importance sampling is carried out for the parameters opted, again, with the help of the virtual least-squares solutions. The importance sampler maps the entire solution phase space uniformly, resulting in individual weights that can differ by orders of magnitude for the sample parameter sets. For the MCMC sampler, the weights are typically within one or two orders of magnitude from each other. In both cases, for probabilistic interpretation, the weights need to be normalized by their total sum. After the preconditioning of the proposal probability density

Table 1: The rotation periods, pole longitudes, and pole latitudes retrieved, their 1-σ error estimates, and the true rotation parameters for the simulated cases. We also give the rms-values of the least-squares fit. For the ellipsoid axial ratios, see Table 2.

	P	λ	β	rms
(171) Ophelia	6.665448 ± 0.000007	326.77 ± 1.52	26.51 ± 3.81	0.030
(506) Marion	13.544183 ± 0.000017	259.60 ± 1.64	-18.59 ± 1.37	0.021
(951) Gaspra	7.042034 ± 0.000007	22.03 ± 0.64	17.16 ± 0.71	0.048
G-20 estimate	8.097576 ± 0.000017	51.61 ± 3.23	43.33 ± 3.05	0.021
G-20 true	8.097585	54.76	40.03	
G-21 estimate a	8.163622 ± 0.000027	297.61 ± 2.71	68.15 ± 4.93	0.018
G-21 estimate b	11.285896 ± 0.009095	118.89 ± 5.11	-57.96 ± 12.57	0.039
G-21 true	8.163624	302.66	53.82	
G-22 estimate	4.148190 ± 0.000002	173.89 ± 0.62	-5.72 ± 2.73	0.015
G-22 true	4.148198	359.65	-27.83	
G-23 estimate a	2.377223 ± 0.000050	61.83 ± 3.73	38.35 ± 10.54	0.023
G-23 estimate b	12.317403 ± 0.000484	245.05 ± 3.47	-29.85 ± 11.33	0.021
G-23 true	12.316848	248.23	-25.63	
G-24 estimate	8.374028 ± 0.000035	286.09 ± 2.24	41.22 ± 4.45	0.015
G-24 true	8.374000	291.26	42.35	
GS-LS estimate	10.173939 ± 0.000041	26.80 ± 2.32	57.59 ± 5.16	0.038
GS-PM estimate	10.173960 ± 0.000047	27.55 ± 2.75	58.78 ± 4.99	0.046
GS true	10.173956	25.02	62.89	–

with the virtual observations, the actual MCMC sampling (or MCMC importance sampling) takes only of the order of a second of time for 10^3 sample parameter sets.

There are a number of additional features worth pointing out. First, rotation can take place about the shortest or longest ellipsoid axes. Second, it is useful to set $a = 1$ at all times. Third, as described above in Sec. 2, the phase function is set to reduce to that of the H,G_1,G_2 or H,G_{12} systems for a perfectly spherical asteroid.

Table 2: The axial ratios b/a and c/a retrieved, their 1-σ error estimates, and the true ratios of the simulated cases. For the rotation parameters, see Table 1.

	b/a	c/a
(171) Ophelia	0.787 ± 0.004	0.465 ± 0.042
(506) Marion	1.222 ± 0.008	2.067 ± 0.151
(951) Gaspra	0.610 ± 0.010	0.524 ± 0.025
G-20 estimate	0.816 ± 0.009	0.805 ± 0.010
G-20 true	0.787	0.787
G-21 estimate a	0.878 ± 0.009	0.505 ± 0.074
G-21 estimate b	0.965 ± 0.022	0.620 ± 0.133
G-21 true	0.820	0.585
G-22 estimate	0.760 ± 0.006	0.631 ± 0.004
G-22 true	0.758	0.631
G-23 estimate a	0.912 ± 0.024	0.567 ± 0.053
G-23 estimate b	0.874 ± 0.035	0.579 ± 0.039
G-23 true	0.847	0.584
G-24 estimate	0.863 ± 0.011	0.786 ± 0.018
G-24 true	0.848	0.724
GS-LS estimate	0.721 ± 0.017	0.524 ± 0.056
GS-PM estimate	0.713 ± 0.014	0.567 ± 0.057
GS true	–	–

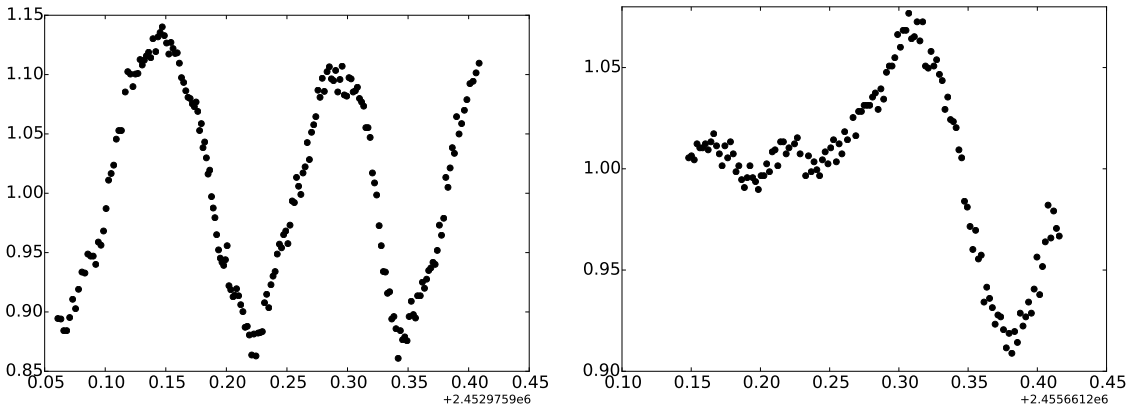

Figure 1: Example lightcurves of (171) Ophelia. For references to the observations, see text.

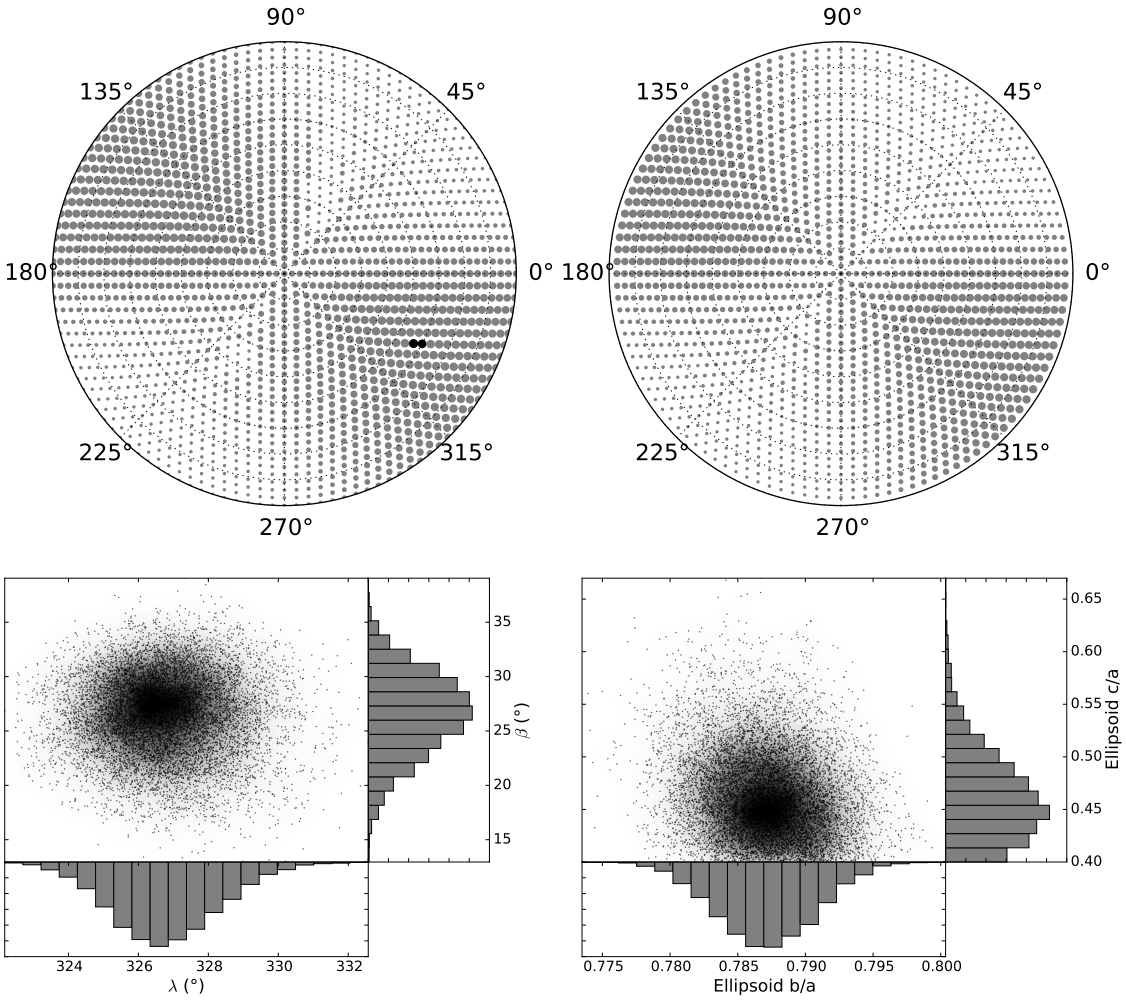

Figure 2: Ecliptic longitude and latitude of the pole scanned for (171) Ophelia with larger bullet size indicating better fits: maps for the northern (top left) and southern ecliptic hemispheres (top right). Black bullets indicate $\Delta\chi^2 < 10$ with respect to the best fit. Also shown are 10,000 MCMC sample poles (bottom left) and sample ellipsoid axial ratios (bottom right) with their one-dimensional marginal distributions.

5. Results and discussion

5.1. Inversion of dense groundbased lightcurves

The inverse methods presented in Sect. 4 have been applied to the lightcurve data of (171) Ophelia, (506) Marion, and (951) Gaspra without the scattering parameters, treating the different lightcurves in the relative sense. For (171) Ophelia, we have used 40 lightcurves, 39 of them documented in [24] and one in [25]. The total timespan of the 2,792 observations is over 28 years. Example lightcurves for Ophelia are shown in Fig. 1.

Our best-fit period is 6.67 hours, and the pole solution is $\lambda = 326°$, $\beta = 30°$. The uncertainty in the pole coordinates is around 5°. The best-fit shape parameters are $b/a = 0.78$ and $c/a = 0.42$. The pole scans and MCMC results are shown in Fig. 2. The rms-value of fit is small, 0.030, which is an excellent fit to dense lightcurve data with the ellipsoid model. The rotation and shape parameters retrieved are given in Tables 1 and 2.

As to the pole scanning in Fig. 2, denoting the least-squares, best-fit solution by $\mathbf{P}_0$, the pole coordinates allowing for solutions

$$\Delta\chi^2 \;=\; \chi^2(\mathbf{P}) - \chi^2(\mathbf{P}_0) \leq 10 \tag{38}$$

are indicated by large black bullets. For deteriorating fits outside these regimes, the grey bullet size is determined by the relation $\exp(-\frac{1}{2}\mathrm{rms}^2/\mathrm{rms}_0^2)$, where rms_0 corresponds to the rms-value of the best-fit solution.

Further in Fig. 2, the scatter plots with kernel estimation show the MCMC samples composed of 10,000 pole coordinates and axial ratios, plotted against each other in pairs, as well as their marginal distributions. A realistic cutoff value of 0.4 has been utilized for the axial ratio, and the c/a distribution can be seen to be limited by the cutoff.

For (506) Marion, we have used 18 lightcurves, some of them documented in [10], others published earlier by [26, 27, 28]. The total timespan of the 2,038 observations is 12.5 years. We acquired a best-fit period of approximately 13.5 hours and a pole solution of $\lambda = 259°$, $\beta = -18°$. The uncertainty in the pole coordinates is around 2°. The asteroid appears to be rotating around its long axis. The axial ratios are therefore approximately $b/a = 1.22$ and $c/a = 2.06$. Example lightcurves for Marion are shown in Fig. 3 and the pole scans and MCMC results are shown in Fig. 4. The rms-value of the fit is very small, 0.021, which is an outstanding fit to dense lightcurve data with the ellipsoid model. The rotation and shape parameters retrieved are given in Tables 1 and 2.

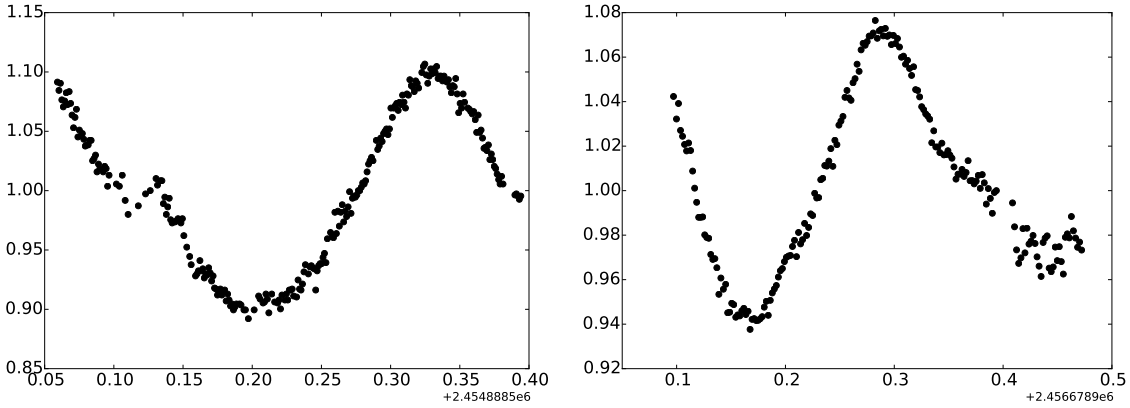

Figure 3: Example lightcurves of (506) Marion. For references to the observations, see text.

For (951) Gaspra, we have used altogether 2,200 observations in 73 different lightcurves, published by [29, 30, 31, 32, 33] and acquired from the DAMIT database [34]. The total timespan is 27.6 years. Example lightcurves for Gaspra are shown in Fig. 5. Our period estimate is approximately 7.04203 hours and the pole solution is $\lambda = 21°$, $\beta = 17°$. The uncertainty in the pole is approximately 1°. The best-fit shape parameters are approximately $b/a = 0.61$, $c/a = 0.52$. These are close to earlier estimates and other shape models. For Gaspra, the b/c and c/a ratios in our MCMC solution were strongly correlated. The pole scans and MCMC results are shown in Fig. 6. The rms-value of fit is 0.048, which is a good fit to the extensive, dense lightcurve data. The rotation and shape parameters retrieved are given in Tables 1 and 2.

Thomas et al. [35] report a pole orientation equivalent to $\lambda = 20°$, $\beta = 21°$ with a 2° uncertainty. We can conclude that our pole orientation with its uncertainty domain intersects with the domain given by Thomas et al. based on the Galileo imaging.

It is notable that the individual rms-values of the lightcurves vary within 0.014-0.134, with typical values below 0.040 and only three rms-values 0.083, 0.102, and 0.134 exceeding 0.072. The slip factors vary between 1.0-3.6, with typical values below 2.5. The present analysis of Gaspra suggests that slip factors are worth utilizing when regular shapes are incorporated in lightcurve inversion for extensively observed asteroids.

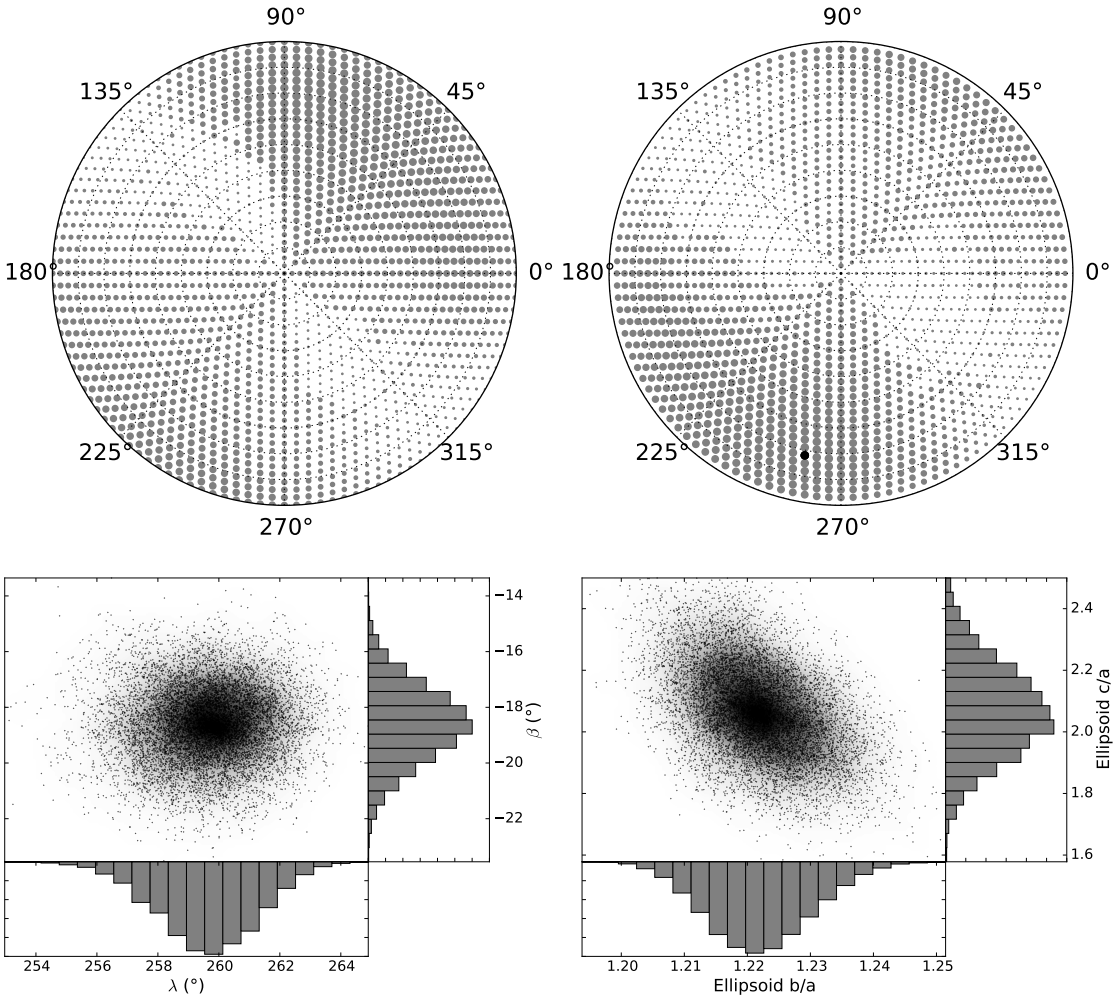

Figure 4: As in Fig. 2 for (506) Marion.

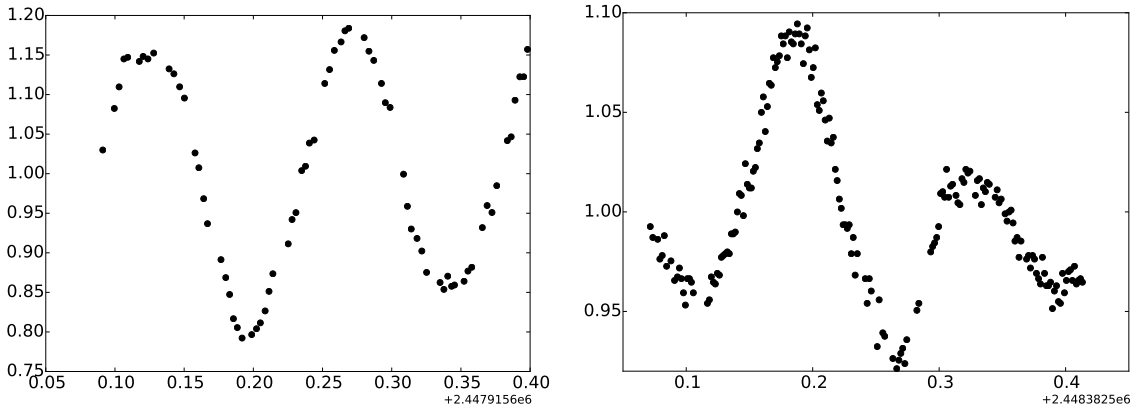

Figure 5: Example lightcurves of (951) Gaspra. For references to the observations, see text.

5.2. Inversion of simulated Gaia photometry

The simulated Gaia photometry consists of altogether seven different simulations of realistic data sets. The first five of them are termed G-20, G-21, ... G-24 and are due to Santana-Ros et al. [7], including 54, 68, 83, 91, and 53 observations, respectively, over a five-year timespan. The remaining two simulations were carried out using an earlier five-year design of the Gaia observational cadence [36, 13] with 69 observations, involving a Gaussian-sphere asteroid [37] with a Lommel-Seeliger reflection coefficient (GS-LS) or a particulate-medium reflection coefficient (GS-PM). For the retrieved and true rotation and shape parameters, see Tables 1 and 2.

The inverse procedures outlined in Sect. 4 were carried out blindly for the data sets G-20, G-21, ... G-24 using the linear phase function of Eq. 16. We emphasize that it was of utmost importance to include a relevant phase function in the analysis: the slope parameter of the linear phase function was optimized and well constrained simultaneously with the other parameters. The rotation and shape parameters retrieved are given in Table 1, next to the true parameter values. Overall, the blind test can be considered successful: the parameters retrieved are in fair agreement with the true values. There are, however, a number of aspects to be assessed.

For G-20, the rotation parameters are in full agreement with the true parameters, whereas the axial ratios show differences. These differences can derive from the choice by Santana-Ros et al. [7] to utilize an approximate geometric treatment of the surface reflection process. Fig. 7 shows that,

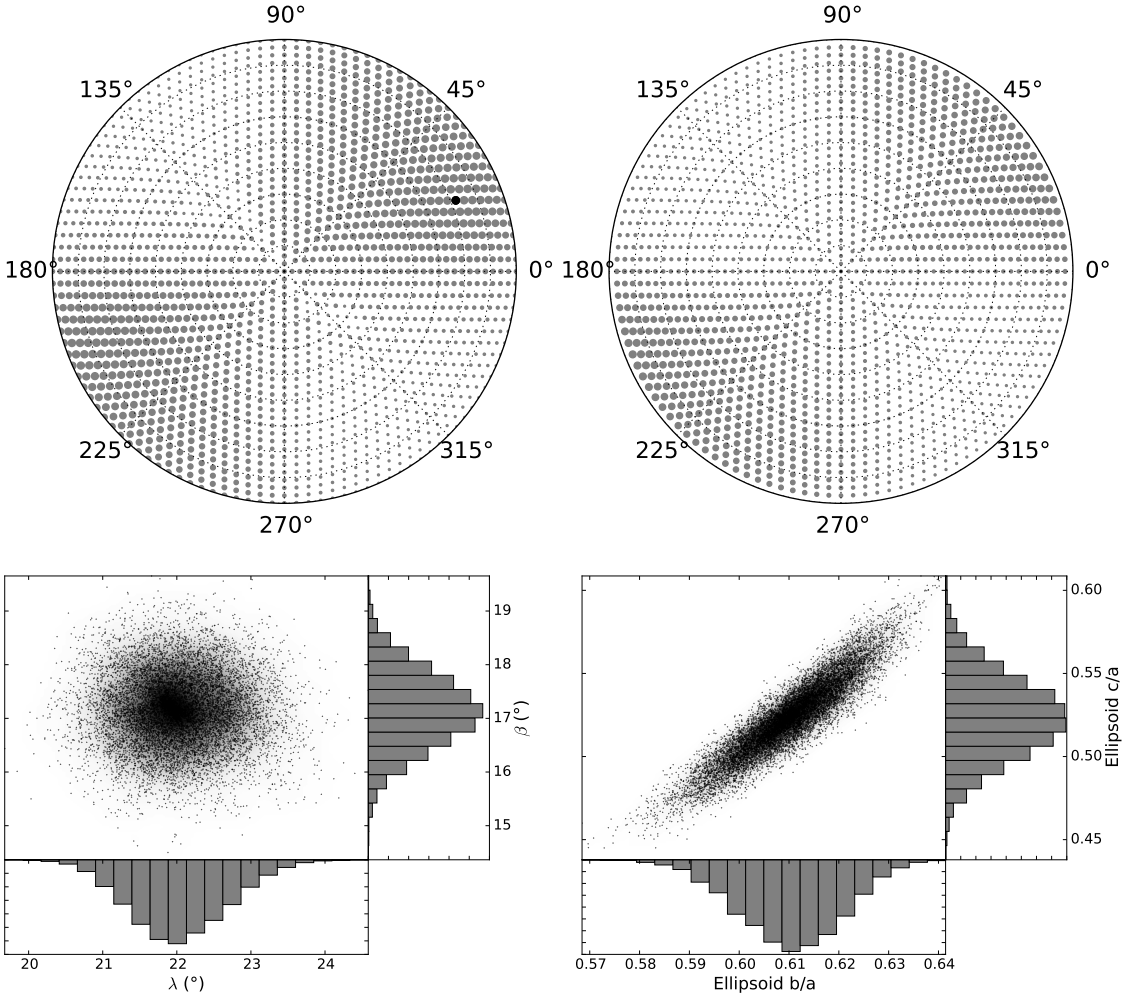

Figure 6: As in Fig. 2 for (506) Marion.

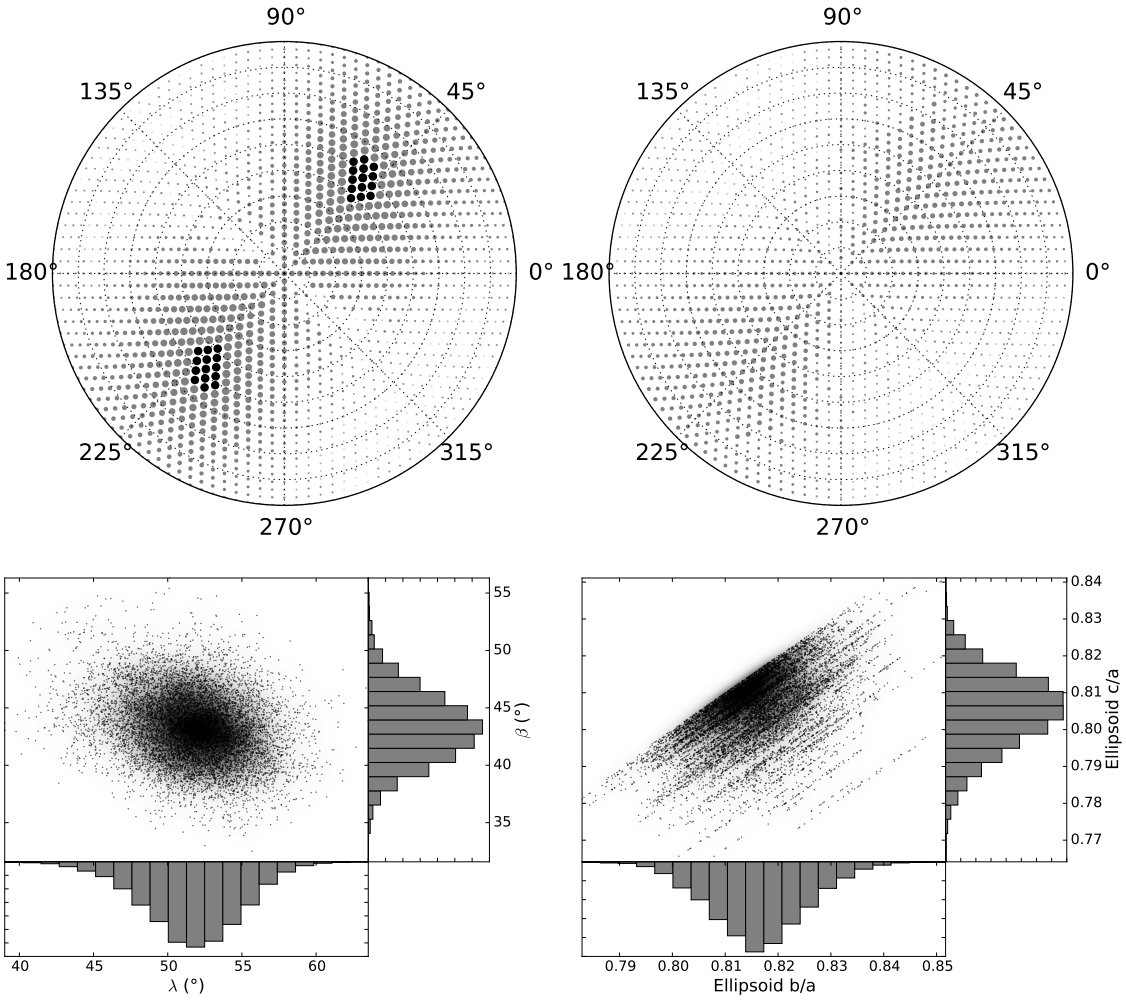

Figure 7: Ecliptic longitude and latitude of the pole scanned for the simulated Gaia asteroid G-20 by Santana-Ros et al. [7] with larger bullet size indicating better fits: maps for the northern (top left) and southern ecliptic hemispheres (top right). Black bullets indicate $\Delta\chi^2 < 10$ with respect to the best fit. Also shown are 10,000 MCMC sample poles (bottom left) and sample ellipsoid axial ratios (bottom right) with their one-dimensional marginal distributions.

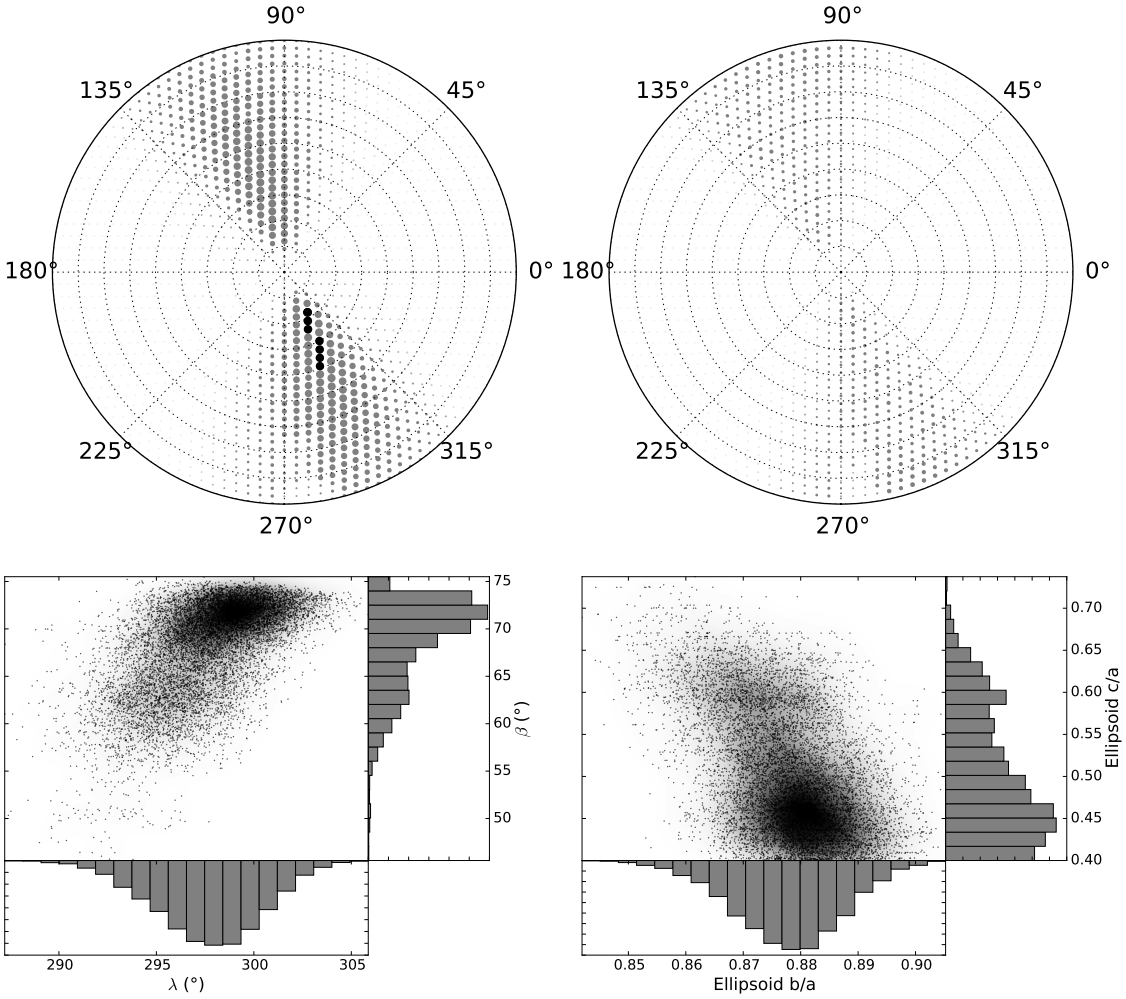

Figure 8: As in Fig. 7 for G-21, case a. See text and Tables 1 and 2.

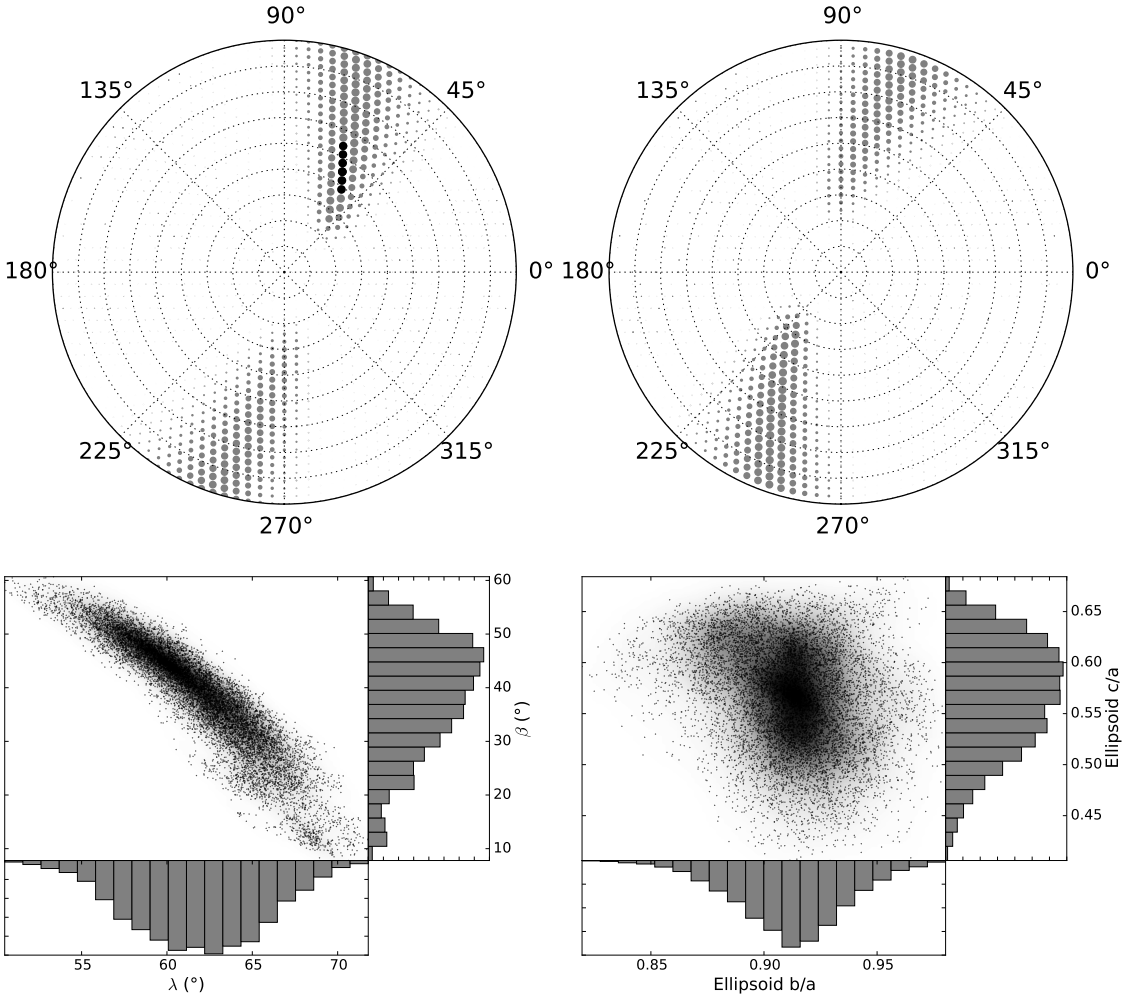

Figure 9: As in Fig. 7 for G-23, case a. See text and Tables 1 and 2.

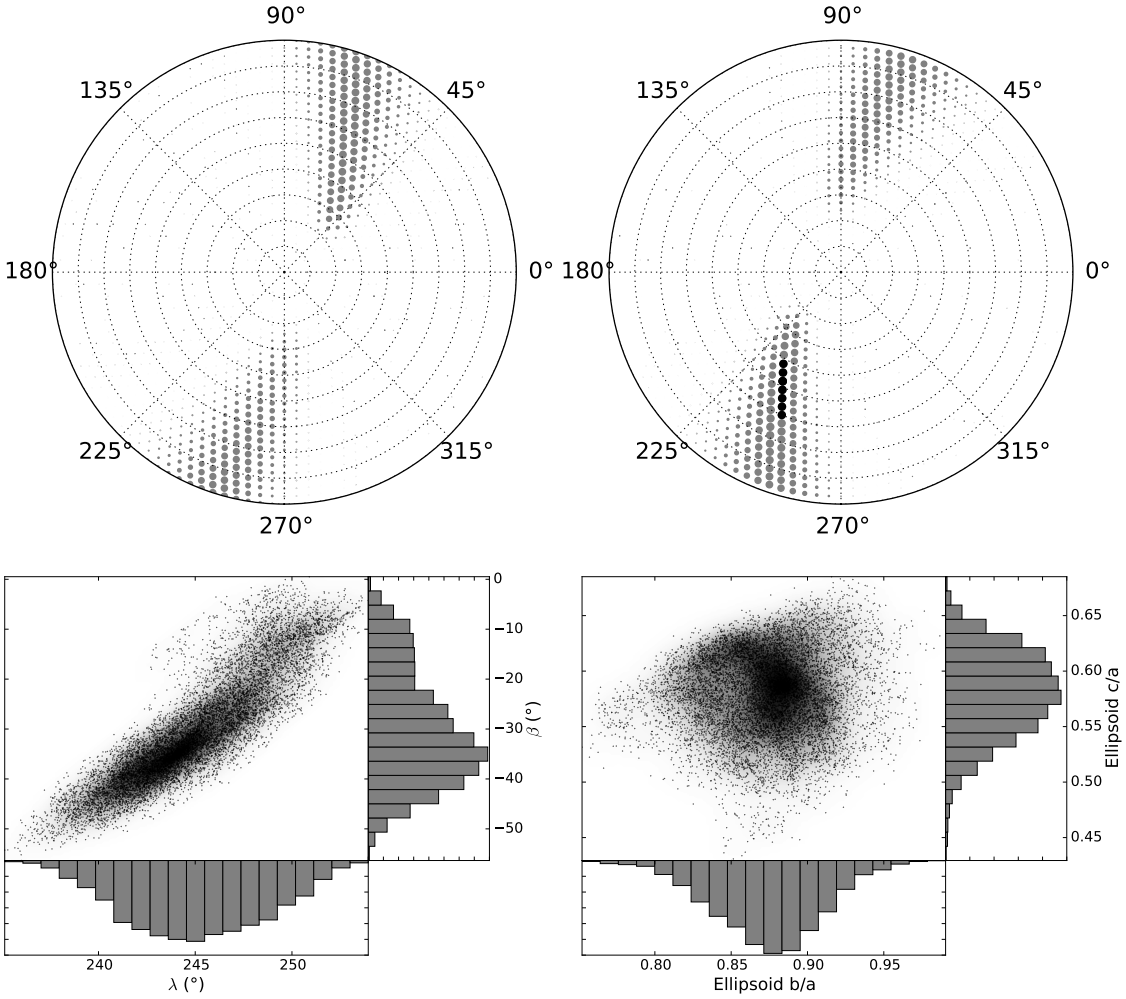

Figure 10: As in Fig. 7 for G-23, case b. See text and Tables 1 and 2.

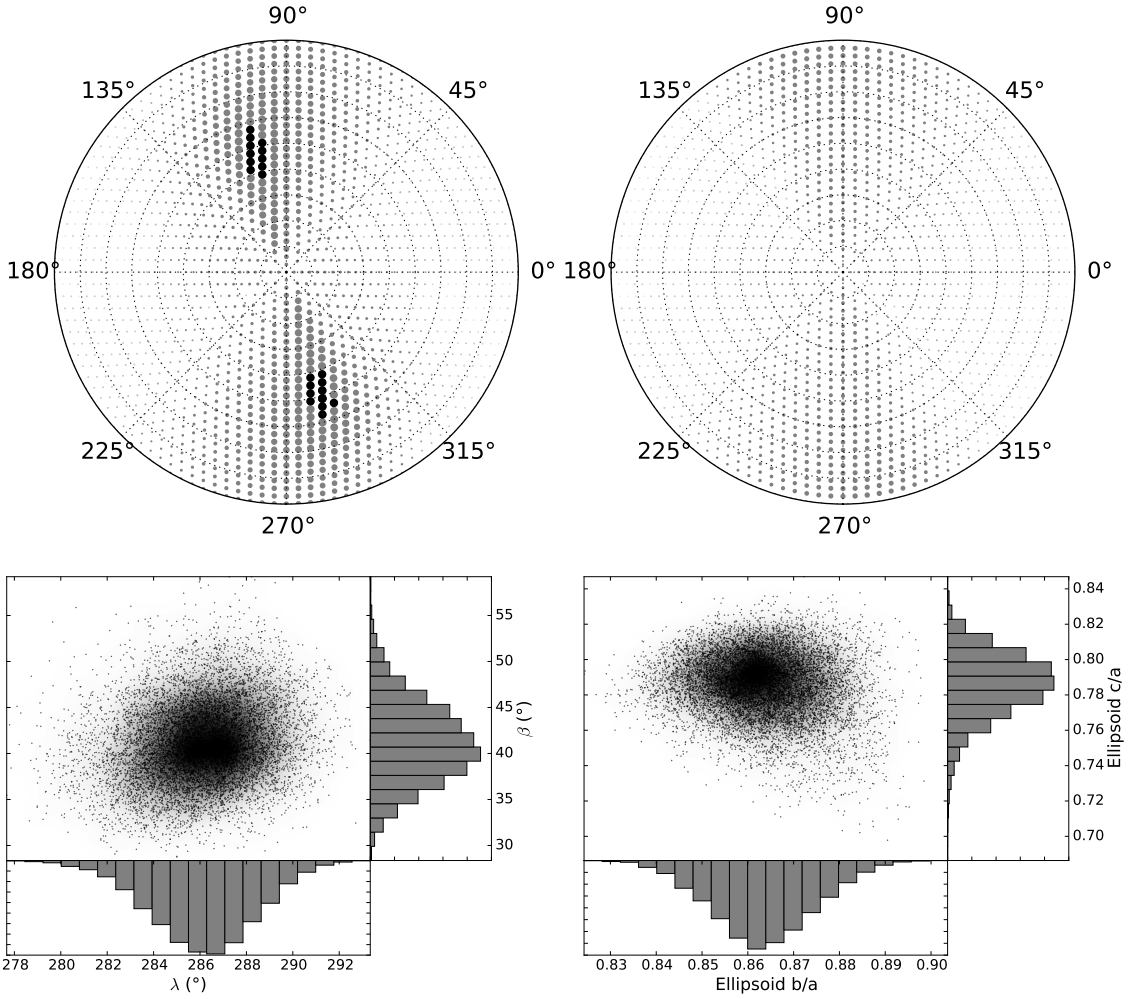

Figure 11: As in Fig. 7 for G-24.

whereas prograde rotation is more probable than retrograde rotation, there are two distinct solutions for the pole longitude. The MCMC sampling for the other pole solution indicates a well-constrained region in the proximity of the best-fit pole. The axial ratios b/a and c/a are close to each other.

For G-21, the rotation period and pole longitude are well retrieved, whereas there are significant differences in the pole latitude and the axial ratios. Fig. 8 indicates that prograde rotation is probable and that the pole longitude $\lambda \approx 300^\circ$ is clearly preferred to the other possibility of $\lambda \approx 120^\circ$. The axis ratio c/a is cut sharply by the preconditioning $c/a > 0.4$ set for inversion. It is possible that certain bimodality is present in the pole latitudes. For G-21, we have analyzed a best-fit local secondary solution for rotation periods larger than 11 h, arising originally from splitting the period scanning into two parallel runs within 2 h $< P <$ 11 h and 11 h $< P <$ 22 h. We note that the secondary solution has a substantially larger rms-value than the primary solution and we do not analyze it further. We note that there may be secondary solutions below 11 h with better rms-values.

For G-22, a typical mirror solution 180° off from the other, true solution is obtained. In this case, it is possible that there is another rotation period, slightly different from the presently retrieved one, that would give the correct pole orientation. For G-23, the latter, slightly better-fitting parameters are completely in agreement with the true parameters. It is, however, illustrative that another solution with only a slightly higher rms-value, corresponds to a different parameter set. Considering the small rms-values, it would probably be impossible to pick up the right solution from the two candidates. One might argue that the shorter period is atypical for asteroids, and, thus, the solution with the longer period would be favored. In Figs. 9 and 10, we illustrate poles scans and MCMC results for both cases. There are clearly only two possible pole longitudes and the axial ratios are similar for the two cases. As to the final example of the blind test, for G-24, the retrieved parameters are in agreement with the true parameters. Based on the pole scan and the MCMC results in Fig. 11, prograde rotation is favored and there are two plausible pole orientations 180° apart.

As to the Gaussian-sphere simulations of the Gaia photometry, results are shown in Figs. 12 and 13 and in Tables 1 and 2. For these direct simulations, realistic surface reflection coefficients with a proper phase functions were utilized. The inverse procedures were carried out with the H,G_{12} phase function, entailing a single parameter for the shape of the phase function (G_{12}). Again, the period scanning indicated the correct prefered rotation

period for both GS-LS and GS-PM. Pole scanning for GS-LS suggested the correct pole as the prefered solution, whereas pole scanning for GS-PM indicated two distinct pole solutions. In general, the retrieval is more ambiguous for the particulate-medium simulation, giving rise to two alternative pole solutions. The G_{12}-parameter was well optimized for both cases.

Careful inspection of Figs. 12 and 13 shows that the MCMC sample clouds are slightly shifted from one another due to the different reflection coefficient utilized in the direct simulation (recall that the inverse procedure utilizes the Lommel-Seeliger coefficient). This note underscores the importance of developing and utilizing realistic reflection coefficients for the particulate surfaces of asteroids.

6. Conclusions

We have shown that the LS-ellipsoid can be efficiently utilized in initial lightcurve inversion for asteroid rotation, shape, and scattering parameters. We have developed robust optimization methods based on the Nelder-Mead simplex algorithm as well as virtual-observation Markov-chain Monte Carlo methods for characterizing the probability density of resulting rotation, shape, and scattering parameters.

The present methods can be further refined as follows. As to the direct methods, first, it is possible to study the natural dependence of LS-ellipsoid phase integrals and spherical albedos on the illumination geometry. Second, the phase curves of ellipsoidal asteroids in random orientation can resemble those for spherical asteroids, enabling a definition of a reference phase curve for a nonspherical asteroid via random orientation. This could provide an alternative, abstract definition of a reference phase curve, earlier considered as the one resulting from equatorial illumination and observation.

As to the inverse methods, first, it can be possible to replace the simplex algorithm with another more efficient yet equally robust algorithm. Second, in order to mitigate the biases due to the regular ellipsoid shape model, it can be possible to derive measures alternative to the present slip-factor treatment for mitigating the a posteriori residual correlations. Third, the inverse methods allow for the retrieval of the scattering parameters pertaining to the H,G_1,G_2 phase function from sparse photometry, which can be of significance in the interpretation of the Gaia photometry.

There are promising future prospects for the present methods. First, we can foresee the replacement of less efficient initial inverse methods in the

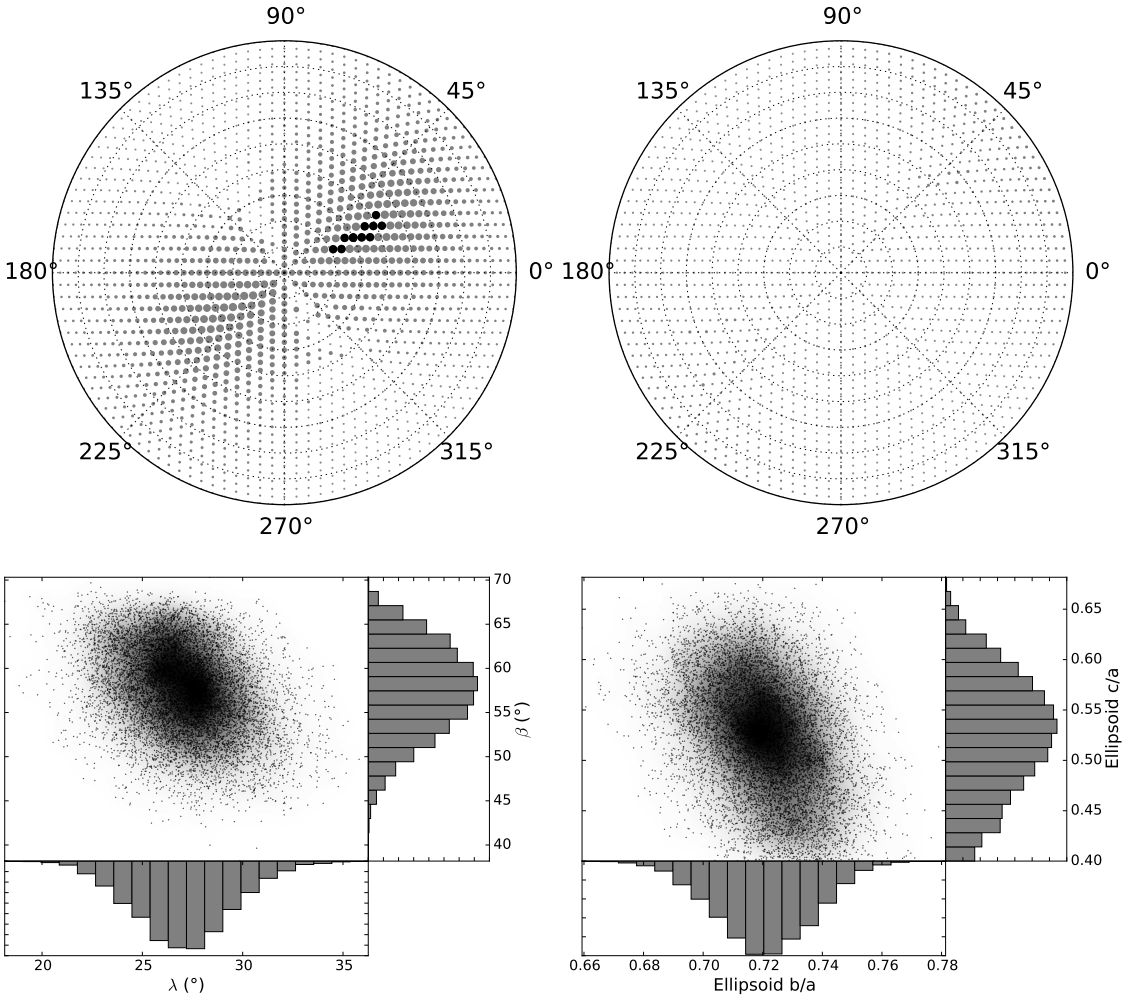

Figure 12: Ecliptic longitude and latitude of the pole scanned for the simulated Gaussian-sphere asteroid with a Lommel-Seeliger reflection coefficient by Torppa and Muinonen [36] with larger bullet size indicating better fits: maps for the northern (top left) and southern ecliptic hemispheres (top right). Black bullets indicate $\Delta\chi^2 < 10$ with respect to the best fit. Also shown are 10,000 MCMC sample poles (bottom left) and sample ellipsoid axial ratios (bottom right) with their one-dimensional marginal distributions.

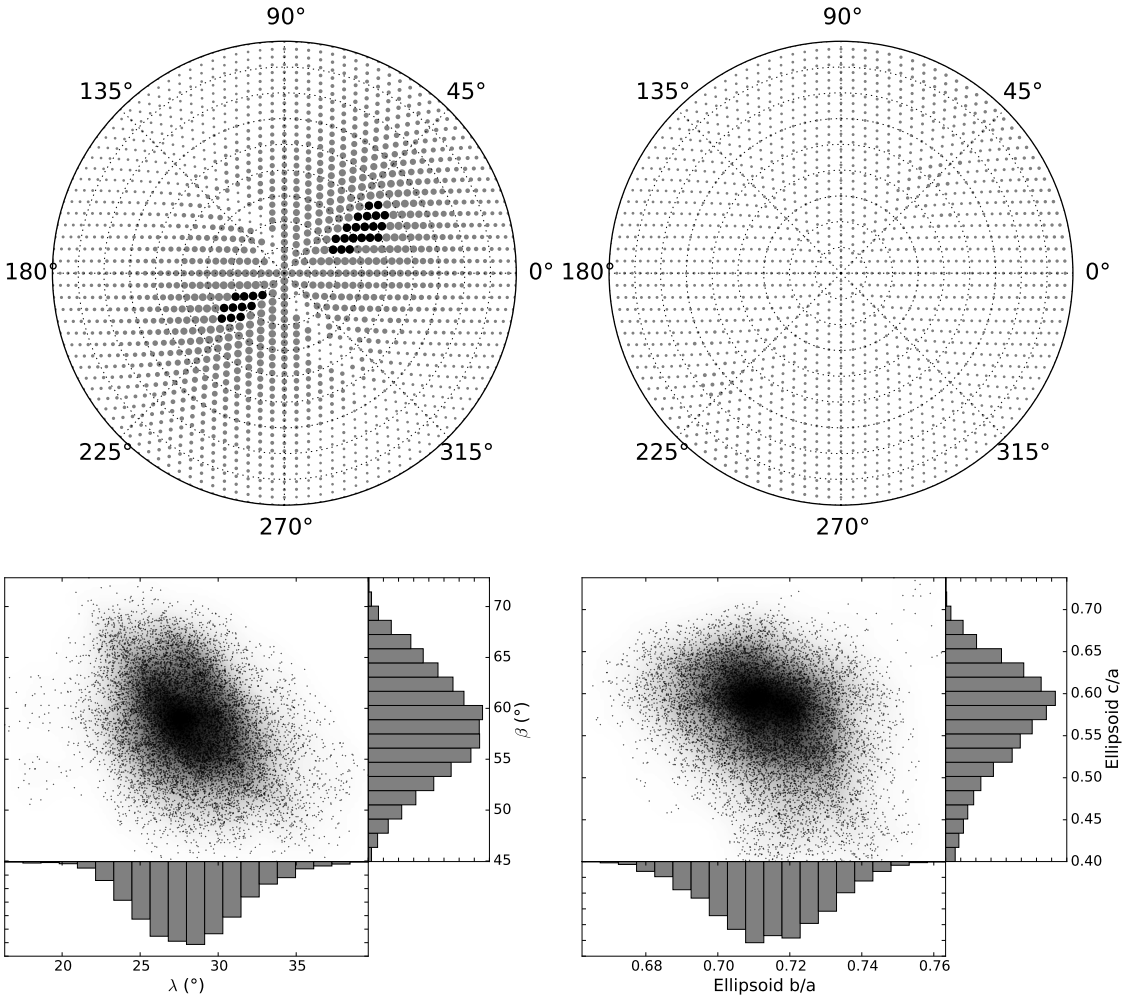

Figure 13: As in Fig. 12 for the Gaussian-sphere asteroid simulated with the numerical particulate-medium reflection coefficient.

conventional lightcurve softwares by those based on the LS-ellipsoid. Second, it is possible to extend the virtual-observation Markov-chain Monte Carlo to lightcurve inversion using general convex shapes.

Acknowledgments. Research supported, in part, by the Academy of Finland (project 1257966).

[1] Kaasalainen, M., Torppa, J., Muinonen, K. 2001. Optimization methods for asteroid lightcurve inversion. II. The complete inverse problem. Icarus 153, 37-51.

[2] Torppa, J., Hentunen, V-P., Pääkkönen, P., Kehusmaa, P., Muinonen, K. 2008. Asteroid shape and spin statistics from convex models. Icarus 198, 91.

[3] Durech, J., Kaasalainen, M., Warner, B. D., Fauerbach, M., Marks, S. A., Fauvaud, S., Fauvaud, M., Vugnon, J.-M., Pilcher, F., Bernasconi, L., Behrend, R. 2009. Asteroid models from combined sparse and dense photometric data. Astron. Astrophys. 493, 291.

[4] Cellino, A., Zappalá, V., Farinella P. 1989. Asteroid shapes and lightcurve morphology. Icarus 78, 298-310.

[5] Lu, X.-P., Ip, W.-H. 2015. Cellinoid shape model for multiple lightcurves. Planet. Space Sci. 108, 31-40.

[6] Cellino, A., Hestroffer, D., Tanga, P., Mottola, S., Dell'Oro, A. 2009. Genetic inversion of sparse disk-integrated photometric data of asteroids: application to Hipparcos data. Astron. Astrophys. 506, 935.

[7] Santana-Ros, T., Bartczak, P., Michalowski, T., Tanga, P., Cellino, A. 2015. Testing the inversion of asteroids' Gaia photometry combined with ground-based observations. Mon. Not. Roy. Astron. Soc. 450, 333-341.

[8] Muinonen, K., Lumme, K. 2015. Disk-integrated brightness of an ellipsoidal asteroid with a Lommel-Seeliger scattering surface. Astron. Astrophys., submitted.

[9] Cellino, A., Muinonen, K., Hestroffer, D., Carbognani, A. 2015. Inversion of sparse photometric data of asteroids using triaxial ellipsoid shape

models and a Lommel-Seeliger scattering law. Planet. Space Sci., submitted.

[10] X. Wang, K. Muinonen, and Y. Wang (2015). Photometric analysis for the spin parameters and shapes of asteroids (362) Havnia and (506) Marion. Planet. Space Sci., submitted.

[11] Muinonen, K., Granvik, M., Oszkiewicz, D., Pieniluoma, T., Pentikäinen, H., 2012. Asteroid orbital inversion using a virtual-observation Markov-chain Monte Carlo method. Planet. Space Sci. 73, 15-20.

[12] Muinonen, K., Fedorets, G., Pentikäinen, H., Pieniluoma, T., Oszkiewicz, D., Granvik, M., Virtanen, J., Tanga, P., Mignard, F., Berthier, J., Dell'Oro, A., Carry, B., Thuillot, W. 2015. Asteroid orbits with Gaia using random-walk statistical ranging. Planet. Space Sci., submitted.

[13] Wilkman, O., Muinonen, K., Peltoniemi, J. I. 2015. Photometry of dark atmosphereless planetary bodies: an efficient numerical model Planet. Space Sci., submitted.

[14] Muinonen, K., Parviainen, H., Näränen, J., Josset, J.-L., Beauvivre, S., Pinet, P., Chevrel, S., Koschny, D., Grieger, B., Foing, B. 2011. Lunar mare single-scattering, porosity, and surface roughness properties with SMART-1/AMIE. Astron. Astrophys. 531, A150, 1-8, doi: 10.1051/0004-6361/201016115.

[15] Parviainen, H., Muinonen, K. 2007. Rough-surface shadowing for self-affine random rough surfaces. J. Quantitat. Spectrosc. Radiat. Transf. 106, 398-416.

[16] Parviainen, H., Muinonen, K. 2009. Bidirectional reflectance of rough particulate media: ray-tracing solution. J. Quantitat. Spectrosc. Radiat. Transf. 110, 1418-1440.

[17] Muinonen, K., Belskaya, I. N., Cellino, A., Delbò, M., Levasseur-Regourd, A.-C., Penttilä, A., Tedesco, E. F. 2010. A three-parameter magnitude phase function for asteroids. Icarus 209, 542-555.

[18] Lumme, K., Bowell, E. 1981. Radiative Transfer in the Surfaces of Atmosphereless Bodies. I. Theory. Astron. J. 86, 1694-1704.

[19] Chandrasekhar, S. 1960. Radiative Transfer, Dover, New York (1960)

[20] Muinonen, K., Bowell, E. 1993. Asteroid orbit determination using Bayesian probabilities. Icarus 104, 255-279.

[21] O'Hagan, A., Forster, J. 2004. Kendall's Advanced Theory of Statistics, Volume 2B, Bayesian Inference, Second Edition, Arnold.

[22] Oszkiewicz, D., Muinonen, K., Virtanen, J., Granvik, M., Bowell, E. 2012. Modeling collision probability for Earth-impactor 2008 TC_3. Planet. Space Sci. 73, 30-38.

[23] Press, W. H., Teukolsky, S. A., Vetterling, W. T., Flannery, B. P. 1992. Numerical Recipes in Fortran 77. The Art of Scientific Computing, 2nd Edition, New York, Cambridge University Press.

[24] Wang, X., Muinonen, K., Wang, Y., Behrend, R., Goncalves R., Oey, J., Antonini, P., Demeautis, C., Manzini, F., Damerdji, J., Montier, J., Klotz, A., Leroy, A., Ganand, G. 2015. Photometric analysis for the spin and shape parameters of the C-type main-belt asteroids (171) Ophelia and (360) Carlova. In preparation.

[25] Tedesco, E. F. 1979. Binary asteroids — Evidence for their existence from lightcurves. Science 203, 905-907.

[26] Robinson, L., Warner, B. D. 2002. Minor Planet Bull. 29, 6.

[27] Warner, B. D. 2009. Minor Planet Bull. 36, 109.

[28] Warner, B. D. 2010. Minor Planet Bull. 37, 127.

[29] Di Martino, M., Ferreri, W., Fulchignoni, M., de Angelis, G., Barucci, M. A. 1990. 66 Maja and 951 Gaspra — Possible flyby targets for Cassini and Galileo missions. Icarus 87, 372-376.

[30] Blanco, C., di Martino, M., Ferreri, W., Gonano, M., Mottola, S., Neukum, G. 1991. Photoelectric and CCD photometry of 951 Gaspra Adv. Space Res. 11, 12, 193-196.

[31] Goldader, J. D., Tholen, D. J., Cruikshank, D. P., Hartmann, W. K. 1991. Galileo support observations of Asteroid 951 Gaspra. Astron. J. 102, 1503-1509.

[32] Mottola, S., di Martino, M., Gonano-Beurer, M., Hoffmann, H., Neukum, G. 1992. Ground-based observations of 951 Gaspra: CCD lightcurves and spectrophotometry with the Galileo filters. Lunar and Planetary Inst., Asteroids, Comets, Meteors 1991, 421-424.

[33] Wisniewski, W. Z., Barucci, M. A., Fulchignoni, M., De Sanctis, C., Dotto, E., Rotundi, A., Binzel, R. P., Madras, C. D., Green, S. F., Kelly, M. L., Newman, P. J., Harris, A. W., Young, J. W., Blanco, C., di Martino, M., Ferreri, W., Gonano-Beurer, M., Mottola, S., Tholen, D. J., Goldader, J. D., Coradini, M., Magnusson, P. 1993. Ground-based photometry of asteroid 951 Gaspra. Icarus 101, 213-222.

[34] Durech, J., Sidorin, V., Kaasalainen, M. 2010. DAMIT: a database of asteroid models. Astron. Astrophyss 513, A46.

[35] Thomas, P. C., Veverka, J., Simonelli, D., Helfenstein, P., Carcich, B., Belton, M. J. S., Davies, M. E., Chapman, C. 1994. The Shape of Gaspra. Icarus 107, 2336.

[36] Torppa, J., Muinonen, K. 2005. Statistical inversion of asteroid spins and shapes from Gaia photometry. In: Three-Dimensional Universe with Gaia, ESA Special Publications SP-576 (C. Turon, K. S. O'Flaherty, and M. A. C. Perryman, Eds., ESA Publications Division, ESTEC, The Netherlands), 321-324.

[37] Muinonen, K. 1998. Introducing the Gaussian shape hypothesis for asteroids and comets. Astron. Astrophys. 332, 1087-1098.